Applied Energy 316 (2022) 119098

Contents lists available at ScienceDirect

Applied Energy

journal homepage: www.elsevier.com/locate/apenergy

Decoding the optimal charge depletion behavior in energy domain for predictive energy management of series plug-in hybrid electric vehicle

Wei Zhou [a,*], Xuan Cai [a], Yaoqi Chen [a], Junqiu Li [b], Xiaoyan Peng [a,*]

[a] School of Mechanical and Vehicular Engineering, Hunan University, People's Republic of China
[b] School of Mechanical and Vehicular Engineering, Beijing Institute of Technology, People's Republic of China

HIGHLIGHTS

- An analytical optimal energy management policy is derived for a series plug-in hybrid electric vehicle.
- Four aggregated optimal charge depletion behaviors are revealed through rigorous theoretical analysis.
- The intrinsic and extrinsic mechanisms behind the optimal charge depletion behaviors are explained.
- An energy-domain SoC planning approach that intelligently exploits driving data statistics based on identified charge depletion behaviors are proposed.

ARTICLE INFO

Keywords:
Predictive energy management
SoC planning
Charge depletion behavior
Plug-in hybrid electric vehicle
Pontryagin's minimum principle

ABSTRACT

A critical issue for designing predictive energy management (PEM) strategy of Plug-in Hybrid Electric Vehicles is the planning of optimal global charge trajectory. Existing planning methods have flaws in terms of optimality or computational efficiency due to their lack of in-depth consideration about optimal charge depletion behaviors. To address this issue, rigorous theoretical analysis on the aggregated local and global optimal charge depletion behaviors in energy domain is conducted by combining Pontryagin's Minimum Principle-based analytical derivations and some qualitative reasoning. Fundamental understanding on how the optimal charge depletion rates behave in different driving conditions and why they exhibit such behaviors is provided. The theoretical analysis is further validated through model-in-the-loop tests using an experimentally validated high-fidelity vehicle simulator. The insights gained from the analysis of this paper establish a fundamental knowledge foundation and may pave a new path for more scientific PEM design in the future.

1. Introduction

With recent advancement in intelligent transportation system (ITS) and vehicle connectivity, it becomes viable to predict upcoming trip information such as traffic flow speed, speed limit and road terrain [1]. Incorporating these information into Energy Management (EM) of Plug-in hybrid electric vehicles (PHEVs), commonly termed as Predictive Energy Management (PEM), has been demonstrated to have potential to significantly improve their fuel economy [2,3].

1.1. Literature review

Many approaches have been proposed in the literature to solve the PEM problem. We briefly classify these approaches into three categories. The first one is to directly generate the optimal control policies at each sampling time using Dynamic Programming (DP), by incorporating trip information predicted either based on a simplified traffic model [4] or a more complex driving cycle reconstruction method [5]. It is challenging to implement this approach in real time due to DP's heavy computation burden, even when exploiting some heuristic techniques to narrow down the search space of the algorithm [6] or simplify the powertrain model [7].

Abbreviations: PEM, Predictive Energy Management; PHEV, Plug-in Hybrid Electric Vehicle; PMP, Pontryagin's Minimum Principle; SoC, State of Charge; ITS, Intelligent Transportation System; EM, Energy Management; DP, Dynamic Programming; SQP, Sequential Quadratic Programming; ECMS, Equivalent Consumption Minimization Strategy; MPC, Model Predictive Control; NN, Neural Network; PSO, Particle Swarm Optimization; SDP, Stochastic Dynamic Programming; APU, Auxiliary Power Unit; BU, Basic Unit; CDR, Charge Depletion Rate; MiL, Model in the Loop.

* Corresponding authors at: 1 Lushan South Rd, Lushan District, Changsha City, Hunan Province 410082, People's Republic of China.
E-mail addresses: zhouwei_bit@sina.com (W. Zhou), xiaoyan_p@126.com (X. Peng).

https://doi.org/10.1016/j.apenergy.2022.119098
Received 30 December 2021; Received in revised form 10 March 2022; Accepted 6 April 2022
Available online 11 April 2022

Nomenclature

P_{apu}	output power of APU [kW]
$\dot{m}_f$	instantaneous fuel rate [g/s]
η_{apu}	APU efficiency [/]
Q_{lhv}	lower heating value of fuel [kJ/g]
η_{apu}^{max}	maximum APU efficiency [/]
$m_{f,idle}$	idle fuel rate [g/s]
V_{oc}	battery open circuit voltage [V]
R_0	battery ohmic internal resistance [Ω]
Q_{nom}	battery nominal capacity [Ah]
P_{wh}	demanded power at driving wheels [kW]
η_m	traction motor efficiency [/]
η_g	gear box efficiency [/]
η_f	final drive efficiency [/]
P_{brk}	mechanical braking power [kW]
δ	equivalent inertial coefficient [/]
m	vehicle cargo mass [kg]
f	tire friction coefficient [/]
g	gravity acceleration [ms^{-2}]
α	road grade [/]
ρ_a	air density [kg/m^3]
C_d	aerodynamic coefficient [/]
A	drag force area [m^2]
V	vehicle velocity [m/s]
$P_{apu,max}$	maximum output power of APU [kW]
SoC_{lb}	lowest boundary of SoC [/]
SoC_{hb}	highest boundary of SoC [/]
λ	co-state [/]
P_M	threshold power for APU activation [kW]
Q_{dmd}	cumulative demanded driving energy [MJ]
sq_e	instantaneous CDR of pure electric mode [J^{-1}]
sq_h	instantaneous CDR of hybrid electric mode [J^{-1}]
$P_{dmd,e}$	demanded electric power of traction motor in electric mode [kW]
$P_{dmd,h}$	demanded electric power of traction motor in hybrid mode [kW]
$\overline{P_{dmd}^{+}}$	average positive demanded power [kW]
$\overline{P_{dmd,bu}^{+}}$	average positive demanded power over a BU [kW]
$\overline{P_{dmd,i}^{+}}$	average positive demanded power over BU i [kW]
$\Delta Q_{dmd,i}$	Q_{dmd}'s variation over BU i [MJ]
ΔSoC_i	SoC's variation over BU i [/]
SoC_0	initial SoC [/]

The second approach is to periodically estimate the optimal co-state in Pontryagin's Minimum Principle (PMP)-based EM strategy or the optimal equivalence factor in Equivalent Consumption Minimization Strategy (ECMS) using updated trip prediction, motivated by the fact that the co-state is the only control parameter related to global driving conditions in the PMP-based strategies. For example, utilizing predicted velocity and road grade profiles, Zhang *et al.* [8] and Zhou *et al.* [9] employed backward shooting and pseudospectral optimization respectively to estimate the co-state. This approach is computationally cheaper than the first one. However, as the optimal control solution (especially the terminal state of charge of battery) is very sensitive to the value of co-state, the performance of this approach would deteriorate significantly if the trip prediction is not accurate enough [10], which is hard to guarantee considering the dynamic change of traffic condition and driving behavior. Increasing the updating frequency of the co-state estimation may alleviate this issue, but it will bring the computational issue again.

A more practical and also popular idea is to repetitively generate optimal reference State of Charge (SoC) profiles according to predicted trip information, and then feedback-based strategies can be employed to track these references. In this kind of approaches, many practices assumed linear depletion of battery SoC with travelled distance. For instance, Stefano *et al.* generated reference trajectory by assuming linear consumption of SoC with mileage, followed by a rule-based torque assignment mechanism for tracking [11]. Guo *et al.* proposed a linear SoC reference generator to direct the lower-level power-split controller [12]. In addition, Xie *et al.* [13] and Tang *et al.* [14] utilized linearly depleted SoC area to determine the upper and lower boundaries for the design of lower-level Model Predictive Control (MPC) strategy. However, in fact, the quasi-linear pattern of optimal SoC trajectories in spatial domain only exhibits in scenarios with similar driving conditions. For trips with distinct driving conditions, especially those with hilly terrains, the control performance by tracking a spatial-domain linear SoC profile is far from optimum [15]. To overcome this shortcoming, intuitive correction rules were suggested in [15] and [16], and a simple heuristic approach for fixed driving route was introduced in [17], where good performance cannot be guaranteed due to the absence of optimization. Therefore, optimization-based SoC planning methods have attracted much attention in recent years.

A major obstacle for the optimization-based SoC planning is its real time implementation. To relief this issue, one way was to offload computationally intensive optimal control algorithms such as Stochastic Dynamic Programming (SDP) to the cloud [18]. However, this technology has strict criteria for load and efficiency of data transmission, as well as information timeliness. Another idea would be to move the computationally intensive tasks offline. For example, neural networks (NNs) were trained offline to map point-wise SoC trajectories with representative driving parameters using optimization results based on PMP [19] or DP [20]. Then, the SoC reference was estimated online according to real-time driving conditions. Likewise, in [21], segment-wise energy demands were predicted from several driving parameters using an offline-trained NN as well and then the SoC profile of each segment was assumed to decline with a constant rate proportional to its average energy demand. Alternatively, Schori *et al.* chose to parse solutions obtained by offline optimizations into look-up tables for online generation of reference SoC trajectories [22]. Pourbafarani *et al.* developed a traffic-based SoC reference builder based on the heuristic control map formed of clustered optimum solution solved by off-line DP [23]. Successful implementation of these techniques depends strongly on the richness of real-world driving data used for the offline training, which is difficult to ensure in practice. To overcome this issue, reference SoC trajectories were directly generated using modified PMP algorithms and sparse traffic predictions [24,25]. A drawback of these algorithms is that their computational burden increases with trip time duration instead of trip length, which would be problematic for journeys with low driving velocity. Therefore, spatial-domain methods are more preferred. With this regard, a route segment-based optimization problem for generating discrete SoC nodes was formulated in [26] and solved using Particle Swarm Optimization (PSO) algorithm. A spatial domain DP algorithm was also proposed to realize the SoC planning in [27], where the predicted trip condition was partitioned into multiple driving patterns with different energy consumption properties [28]. These methods are still computationally demanding since large-scale dynamic optimization is needed for the SoC planning.

In our previous work [29], we proposed an energy-based analytical SoC planning method, which was inspired by a quasi-linear pattern between accumulated driving energy and SoC. This method is computationally very cheap as only simple analytical formulas are used.

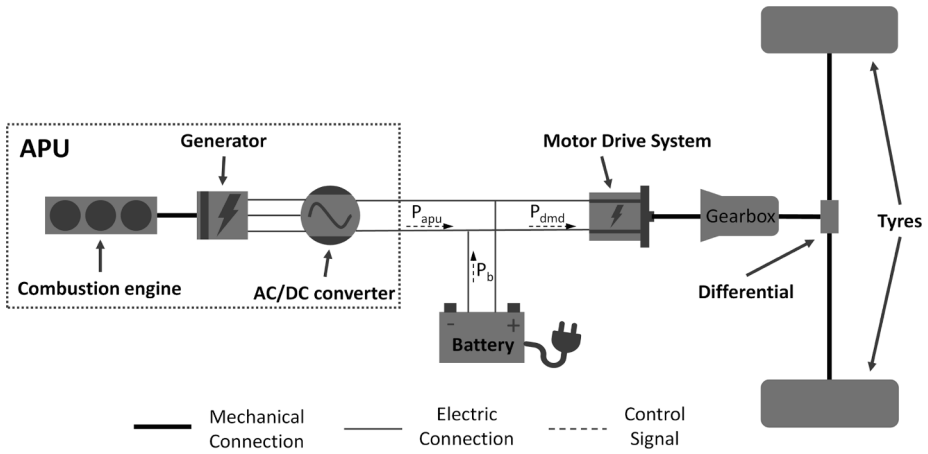

Fig. 1. Configuration scheme of the series PHEV. The primary components and parameters of the power system are as follows: the nominal power of engine-generator set (APU) is 75 kW; the nominal power of permanent magnet synchronous motor is 130 kW, and the peak power is about 170 kW; the nominal energy capacity of lithium-ion battery pack is 140 Ah (59 kWh). The gearbox has two gears whose shifting is controlled by velocity-dependent rules as presented in [9].

Nevertheless, in [29], the quasi-linear pattern in energy domain was found merely through limited numerical experiments instead of theoretical justifications, restricting its credible application to various driving scenarios. In other words, this method will loss optimality in certain driving scenarios due to its assumption of quasi-linear charge depletion in energy domain.

1.2. Knowledge gap and original contribution

As summarized above, although numerous planning approaches have been proposed in the literature, they are either far from global optimum or computationally heavy. The underlying reason is that those approaches lack in-depth consideration about the optimal behavior of charge depletion, *i.e.*, the shape of the optimal SoC trajectory and the dominant factors that influence the shape. In order to address this issue, we provide fundamental understanding on how the optimal charge depletion rates behave in different driving conditions and why they exhibit such behaviors in this paper.

Two unique contributions are made in this paper. First, four aggregated optimal charge depletion behaviors are revealed through rigorous theoretical analysis based on an analytical optimal energy management policy derived by Pontryagin's Minimum Principle. The intrinsic and extrinsic mechanisms behind these behaviors are explained. Second, an energy-domain SoC planning approach that intelligently exploits driving data statistics based on identified charge depletion behaviors are proposed. The insights gained from this paper paves a new road for more scientific design of PEM algorithms in the future.

1.3. Material organization

The remainder of this paper is organized as follows. Section 2 summarizes the formulation of the optimal EM problem. Section 3 presents an analytical solution to the optimal EM problem and details the theoretical analysis of the aggregated and global behavior of the energy-domain optimal charge depletion rates. Section 4 validates the analytical solution and the behavior analysis using a high-fidelity vehicle simulator, and presents an approach to SoC planning based on the revealed optimal charge depletion behaviors. Finally, main conclusions are drawn in Section 5.

2. Optimal energy management problem formulation

The investigated vehicle is a plug-in hybrid electric bus with series powertrain configuration as illustrated in Fig. 1. The major task of the EM strategy is to maximize fuel economy while meeting the demanded driving power [30]. To achieve this goal, an optimal control problem is formulated. Basic elements of the optimal control problem are summarized in the following.

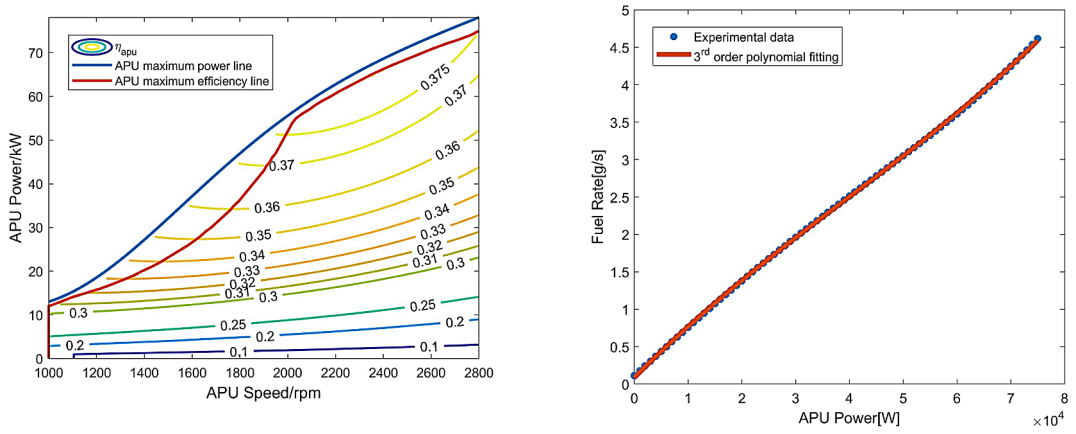

(a) (b)

Fig. 2. (a) Quasi-static efficiency map and maximum efficiency line of the APU system; (b) Instantaneous fuel rates for the maximum efficiency line.

Table 1
Values of related vehicle parameters.

Parameter	Value	Parameter	Value
η_f	0.97	f	0.012
η_g(at 1st gear)	0.93	η_g(at 2nd gear)	0.95
m	14,500	ρ_a	1.225
A	7.67	C_d	0.8
δ(at 1st gear)	1.1268	δ(at 2nd gear)	1.0125

2.1. *Objective* function

The objective function is formulated as the sum of instantaneous fuel rates over the whole driving course:

$$J(P_{apu}(t)) = \int_{t_0}^{t_f} \dot{m}_f(P_{apu}(t))dt = \int_{t_0}^{t_f} \frac{P_{apu}(t)}{\eta_{apu}(P_{apu}(t))Q_{lhv}}dt \tag{1}$$

where P_{apu} is formulated as the control input of the optimal EM problem. As the APU is mechanically decoupled from the vehicle drivetrain, it has the freedom to operate along its maximum efficiency line as shown in Fig. 2(a). Therefore, the instantaneous fuel rate can be calculated by the maximum efficiency according to:

$$\dot{m}_f(P_{apu}(t)) = \frac{P_{apu}(t)}{\eta_{\text{apu}}^{\max}(P_{apu}(t))Q_{lhv}} \tag{2}$$

The instantaneous fuel rates obtained using Eq. (2). are visualized in Fig. 2(b), which also shows that the experimental data is fitted with very good accuracy by a 3rd order polynomial. The polynomial function is expressed as:

$$\dot{m}_f(P_{apu}(t)) = m_{fidle} + k_1 P_{apu}(t) + k_2 P_{apu}^2(t) + k_3 P_{apu}^3(t) \tag{3}$$

where the fitting coefficients,k_1, k_2 and k_3, are 7.3213×10^{-5}, -4.8287×10^{-10} and 4.1035×10^{-15} respectively; $m_{f,idle}$ is the idle fuel consumption and is 0.0808 g/s in this study.

It should be noted that the analytical optimal control policy obtained in Section 3.1 is based on third order polynomial approximation to the experimental data. For APUs with fuel consumption characteristics that can only be approximated by polynomial functions with more than third order, analytical solution to the optimal energy management problem is not possible. Nevertheless, we have verified by numerical solutions that the optimal charge depletion patterns and their influencing mechanisms are still applicable.

2.2. *State* equation

A widely used battery model that represents the battery as an electrical circuit comprised of a voltage source and a purely ohmic impedance is adopted [31,32]. In this model, battery SoC is the only state variable that needs to be optimized and its dynamics is governed by Eq. (4). Note that the influence of temperature on battery parameters is neglected under the assumption of sufficiently good thermal management.

$$\dot{SoC}(t) = -\frac{V_{oc}(SoC(t)) - \sqrt{(V_{oc}^2(SoC(t)) - 4\left(P_{dmd}(t) - P_{apu}(t)\right)R_0(SoC(t))}}{2R_0(SoC(t))Q_{nom}} \equiv f(SoC(t), P_{apu}(t)) \tag{4}$$

where P_{dmd} is the electric power demanded by the traction motor, which can be calculated using the following energy-oriented model [9]:

$$P_{dmd}(t) = \begin{cases} \dfrac{P_{wh}(t)}{\eta_m(t)\eta_g(t)\eta_f}; & P_{wh}(t)\geqslant 0 \\ (P_{wh}(t) - P_{brk}(t))\eta_m(t)\eta_g(t)\eta_f; & P_{wh}(t) < 0 \end{cases} \tag{5a}$$

$$P_{wh}(t) = \left(\delta m\dot{V}(t) + fmg\cos\alpha\left(t\right) + 0.5\rho_a C_d A V(t)^2 + mg\sin\alpha\left(t\right)\right)V(t) \tag{5b}$$

where P_{brk} is the mechanical braking power determined by a maximum-energy-recovery regenerative braking strategy [33]. Values of related vehicle parameters are listed in Table 1.

2.3. *System* constraints

First of all, a terminal state constraint as expressed by Eq. (4) is needed to prevent over-discharge of the battery. In all the simulations of this study, SoC_f is set as 0.3. We note that the value of SoC_f will not influence the analytical derivation in the following section.

$$SoC(t_f) = SoC_f \tag{6}$$

Moreover, some state and control constraints due to physical limits or safety concerns are required to be satisfied:

$$0\leqslant P_{apu}(t)\leqslant P_{apu,\max} \tag{7a}$$

$$SoC_{lb}\leqslant SoC(t)\leqslant SoC_{hb} \tag{7b}$$

$$P_{b,\min}(t)\leqslant P_b(t)\leqslant P_{b,\max}(t) \tag{7c}$$

where $P_{b,\min}$ and $P_{b,\max}$ represent the charging and discharging power capability of the battery, which is respectively restricted by the battery's upper and lower cut-off voltages.

3. Theoretical analysis on the energy-domain optimal charge depletion behavior

In this section, we first derive an analytical solution to the optimal EM problem for the series PHEV powertrain, which is then used to investigate the local and global behavior of the energy-domain optimal charge depletion both qualitatively and quantitatively.

3.1. Analytical solution to the optimal energy management problem

PMP has been widely applied to solve optimal EM problems in the literature, both analytically and numerically. To simplify the analytical derivation of the optimal control solution based on the PMP approach, we hope to relax the state and path constraints as expressed by Eq. (7b) and Eq. (7c). Kim *et al.* has proved that the global optimum is achieved when the SoC gradually decreases to its allowed lowest value just at the end of the whole trip [34], meaning the optimal solution will not violate Eq. (7b). Eq. (7c) should be satisfied as well since a PHEV's battery normally has large capacity with sufficient power capability. Based on the above two justifications, we are assured that the state and path constraints can be relaxed. Therefore, the Hamiltonian function of the optimal EM problem is:

$$H = \dot{m}_f(P_{apu}(t)) + \lambda(t)\dot{SoC}(t) \tag{8}$$

The optimal control input P_{apu}^* can be obtained by minimizing the

Hamiltonian function:

$$P^*_{apu}(t) = \arg_{0\leqslant P_{apu}\leqslant P_{apu,\max}} \min H[SoC^*(t), \lambda^*(t), P_{apu}(t), t] \tag{9a}$$

where the optimal state and co-state variables are governed by:

$$\dot{SoC}^*(t) = \frac{\partial H^*}{\partial \lambda^*} = f(SoC^*(t), P^*_{apu}(t)) \tag{9b}$$

$$\dot{\lambda}^*(t) = -\frac{\partial H^*}{\partial SoC^*} \tag{9c}$$

Due to the existence of the terminal state constraint as expressed by Eq. (6), the above three equations compose a two-point boundary value problem where the most difficult thing is to determine the initial value of the optimal co-state variable. Commonly, trial-and-error shooting method is employed to find the optimal initial co-state, which is computationally very expensive and not suitable for real-time implementation. Therefore, in this paper, we only apply this method to provide an offline benchmark. In the following, we present an analytical solution to the problem described by Eq. (9).

First of all, to facilitate the derivation process, we approximate $\sqrt{V_{oc}^2 - 4R_0(P_{dmd} - P_{apu})}$ by second-order Taylor expansion at $P_{dmd} - P_{apu} = 0$:

$$\sqrt{V_{oc}^2 - 4R_0(P_{dmd} - P_{apu})} \approx V_{oc} - \frac{2R_0}{V_{oc}}(P_{dmd} - P_{apu}) - \frac{2R_0^2}{V_{oc}^3}(P_{dmd} - P_{apu})^2 \tag{10}$$

A comparison between the original function and its Taylor expansion is shown in Fig. 3, validating the accuracy of the approximation.

Substituting Eq. (10) into the state equation and the Hamiltonian function yields:

$$\dot{SoC}(t) \approx -\frac{P_{dmd}(t) - P_{apu}(t)}{V_{oc}(SoC(t))Q_{nom}} - -\frac{R_0(P_{dmd}(t) - P_{apu}(t))^2}{V_{oc}(SoC(t))^3 Q_{nom}} \tag{11}$$

$$H \approx m_{f,idle} + k_1 P_{apu}(t) + k_2 P^2_{apu}(t) + k_3 P^3_{apu}(t) - \frac{\lambda(t)(P_{dmd}(t) - P_{apu}(t))}{V_{oc}(SoC(t))Q_{nom}} - \frac{\lambda(t)R_0(P_{dmd}(t) - P_{apu}(t))^2}{V_{oc}(SoC(t))^3 Q_{nom}} \tag{12}$$

The necessary condition for Eq. (9a) can be obtained from the first derivative of the Hamiltonian function through:

$$\frac{\partial H}{\partial P_{apu}} = k_1 + 2k_2 P_{apu}(t) + 3k_3 P^2_{apu}(t) + \frac{\lambda^*(t)}{V_{oc}(SoC^*(t))Q_{nom}} + \frac{2\lambda^*(t)R_0(P_{dmd}(t) - P_{apu}(t))}{V_{oc}(SoC^*(t))^3 Q_{nom}} = 0 \tag{13}$$

The above equation has two solutions:

$$P_{apu,1} = \frac{-(k_2 - \frac{\lambda^*(t)R_0}{V_{oc}(SoC^*(t))^3 Q_{nom}}) + \sqrt{(k_2 - \frac{\lambda^*(t)R_0}{V_{oc}(SoC^*(t))^3 Q_{nom}})^2 - 3k_3(k_1 + \frac{\lambda^*(t)}{V_{oc}(SoC^*(t))Q_{nom}} + \frac{2\lambda^*(t)R_0P_{dmd}(t)}{V_{oc}(SoC^*(t))^3 Q_{nom}})}}{3k_3} \tag{14a}$$

$$P_{apu,2} = \frac{-(k_2 - \frac{\lambda^*(t)R_0}{V_{oc}(SoC^*(t))^3 Q_{nom}}) - \sqrt{(k_2 - \frac{\lambda^*(t)R_0}{V_{oc}(SoC^*(t))^3 Q_{nom}})^2 - 3k_3(k_1 + \frac{\lambda^*(t)}{V_{oc}(SoC^*(t))Q_{nom}} + \frac{2\lambda^*(t)R_0P_{dmd}(t)}{V_{oc}(SoC^*(t))^3 Q_{nom}})}}{3k_3} \tag{14b}$$

According to the property of quadratic equation, the following inequality should hold:

$$0 < P_{apu,2} < -\frac{k_2}{3k_3} < P_{apu,1} < P_{apu,\max} \tag{15}$$

As the opening of the function $\partial H/\partial P_{apu}$ is upward, its sign is positive when $P_{apu} \in \{[0, P_{apu,2}) \| (P_{apu,1}, P_{apu,\max}]\}$ and is negative when $P_{apu} \in (P_{apu,2}, P_{apu,1})$. This indicates that H increases monotonously with P_{apu} in the interval $[0, P_{apu,2})$ or $(P_{apu,1}, P_{apu,\max}]$, but decreases monotonously with P_{apu} in the interval $[P_{apu,2}, P_{apu,1}]$. Therefore, as can be seen in Fig. 4, the global minimum of H can be either located at $P_{apu} = 0$ or $P_{apu} = P_{apu,1}$.

When $P^*_{apu} = P_{apu,1}$, we should have $H(P_{apu,1}) < H(0)$, according to which the inequality of Eq. (16) can be derived. Note that when deriving this inequality, we used the original Hamiltonian function instead of its approximation since otherwise an inequality that is always satisfied will be resulted in.

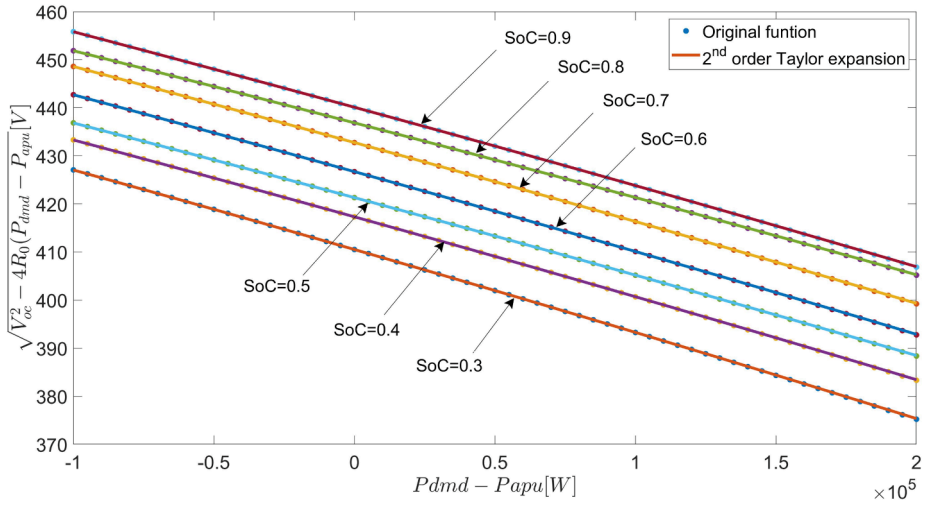

Fig. 3. Comparison of $\sqrt{V_{oc}^2 - 4R_0(P_{dmd} - P_{apu})}$ between the original function and its Taylor expansion.

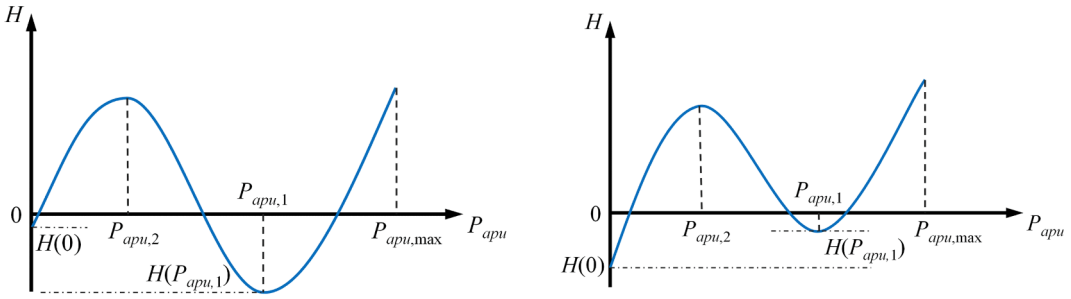

(a) $H(0) > H(P_{apu,1})$ (b) $H(0) < H(P_{apu,1})$

Fig. 4. Two scenarios for the minimum of the Hamiltonian function.

$$P_{dmd} > \frac{1}{4R_0}\left[V_{oc}^2 - \frac{(a-b^2)^2}{4b^2}\right] \equiv P_M \tag{16}$$

where $a = 4R_0P_{apu,1}$,$b = -2R_0Q_{nom}(k_1P_{apu,1} + k_2P_{apu,1}^2 + k_3P_{apu,1}^3)/\lambda^*$.

When $P_{dmd} \leqslant P_M$, the optimal solution is $P_{apu}^* = 0$. In summary, the following optimal control policy exists:

$$P_{apu}^* = \begin{cases} 0, P_{dmd} \leqslant P_M \\ P_{apu,1}, P_{dmd} > P_M \end{cases} \tag{17}$$

To facilitate the analysis later, we present a lemma and a remark in advance regarding the property of the optimal control policy as described by Eq. (17).

Lemma 1: λ^*/V_{oc}^* and $P_{apu,1}$ are both constant.

Proof: After simple mathematical manipulation, we have:

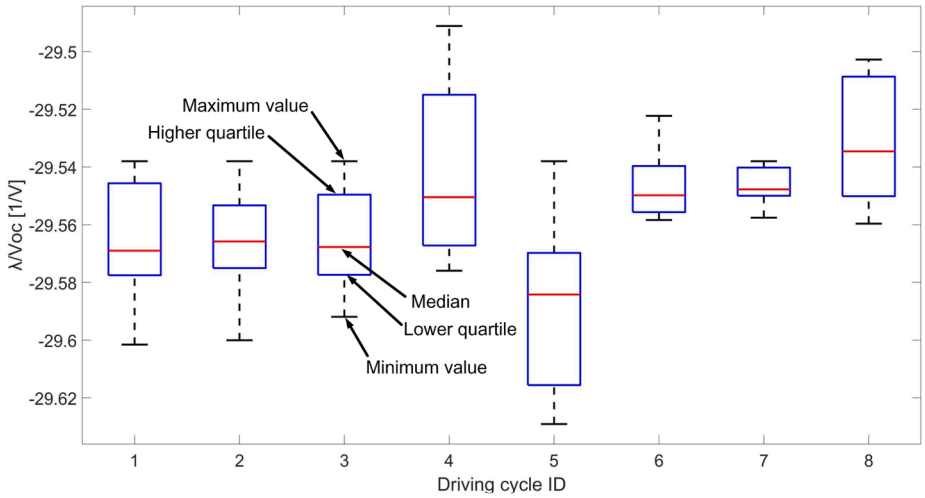

Fig. 5. Boxplot of λ^*/V_{oc}^* values obtained by offline numerical optimization for different driving cycles.

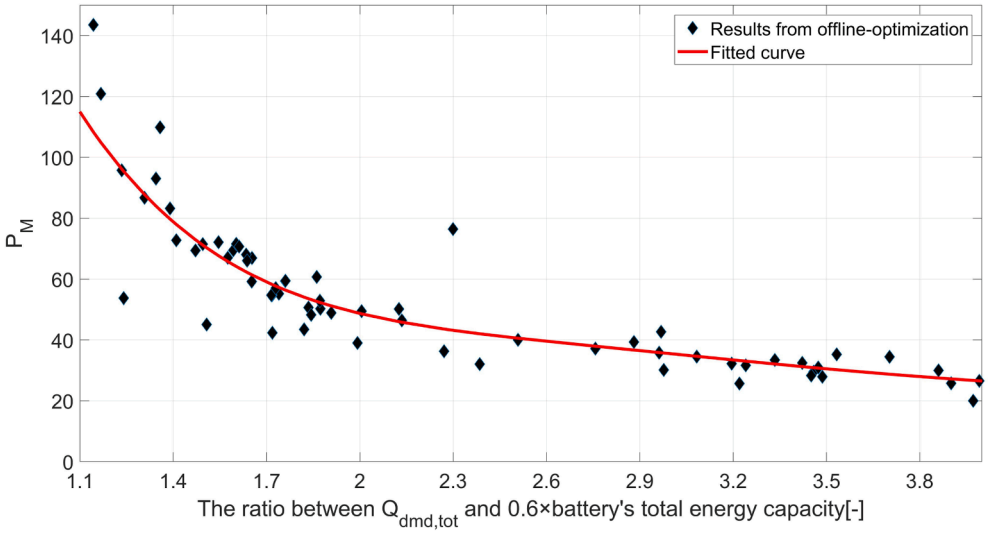

Fig. 6. The correlation between P_M and the vehicle's total driving energy consumption for different driving cycles.

$$\dot{\lambda}^* = \frac{d\lambda^*}{dV_{oc}^*}\frac{dV_{oc}^*}{dSoC^*}\frac{dSoC^*}{dt} \tag{18}$$

Substituting Eq. (11) into Eq. (18) yields:

$$\dot{\lambda}^* = -\frac{d\lambda^*}{dV_{oc}^*}\frac{dV_{oc}^*}{dSoC^*}\frac{P_{dmd}-P_{apu}^*}{V_{oc}^* Q_{nom}}\left(1+\frac{R_0(P_{dmd}-P_{apu}^*)}{V_{oc}^{*2}}\right) \tag{19}$$

On the other hand, by combining Eq. (9c) and Eq. (12), we obtain:

$$\dot{\lambda}^* = -\frac{\lambda^*(P_{dmd}-P_{apu}^*)\frac{dV_{oc}^*}{dSoC^*}}{V_{oc}^{*2}Q_{nom}}\left(1+\frac{R_0(P_{dmd}-P_{apu}^*)}{V_{oc}^{*2}}\right) \tag{20}$$

Comparing Eq. (19) and Eq. (20), the following equality can be further derived:

$$\frac{d\lambda^*}{dV_{oc}^*} = \frac{\lambda^*}{V_{oc}^*} \tag{21}$$

Thus:

$$d\left(\frac{\lambda^*}{V_{oc}^*}\right)/dt = \frac{d\lambda^*\cdot V_{oc}^* - \lambda^* dV_{oc}^*}{V_{oc}^{*2}\cdot dt} = 0 \tag{22}$$

This proves that λ^*/V_{oc}^* is a constant, which, according to Eq. (14(a)), further indicates $P_{apu,1}$ is near constant.

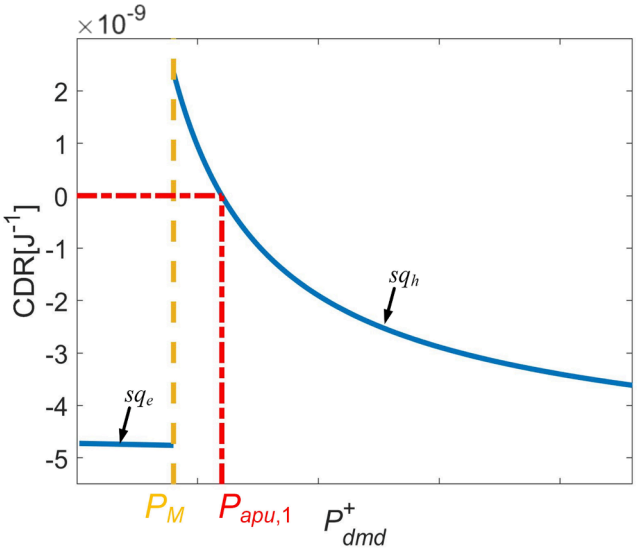

Fig. 8. The relationship between CDR and P_{dmd}^{+}.

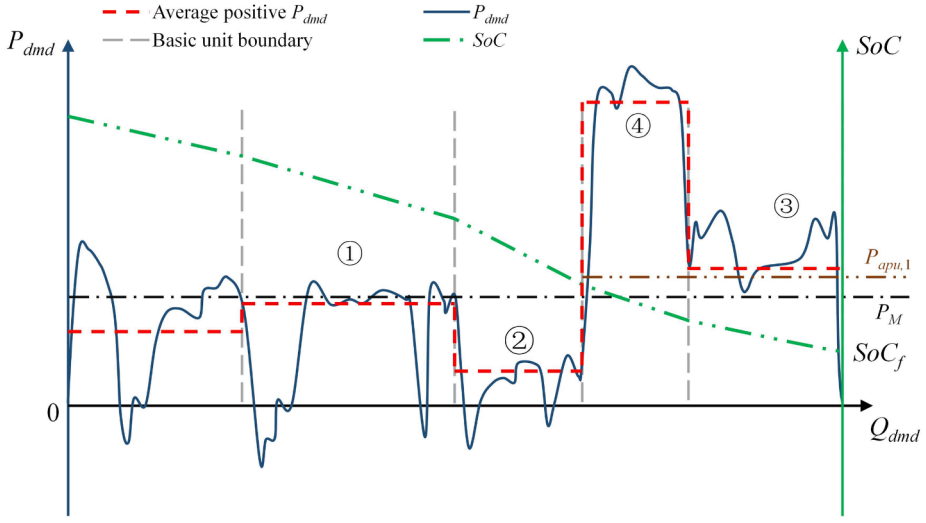

Fig. 7. P_{dmd} trajectory segmented into multiple BUs and the corresponding SoC trajectory in energy domain. P_{dmd} is averaged within each BU as shown by the red dashed line. The charge depletion behavior ('①'~'④') is evaluated according to the relationship between the average value of P_{dmd} within each BU and the magnitude of P_M and $P_{apu,1}$. The approximate trajectory of SoC has a piecewise-linear pattern in energy domain, as related to the charge depletion behavior. (For interpretation of the references to colour in this figure legend, the reader is referred to the web version of this article.)

Lemma 1 implies that the APU works at a constant power once it turns on. In order to further verify this lemma, offline numerical optimizations are performed for 8 different driving cycles. The boxplot of λ^*/V_{oc}^* is shown in Fig. 5, demonstrating that λ^*/V_{oc}^* not only has negligible variation within a driving cycle but also is almost cycle-independent. The offline optimization results also show that the optimal APU power is around 60 kW, very close to the number calculated using Eq. (14(a)).

Remark 1: The threshold variable P_M is correlated with $Q_{dmd,tot}$, the vehicle's total energy consumption for driving. And the larger $Q_{dmd,tot}$ is, the smaller P_M is.

Obviously, $Q_{dmd,tot}$ is proportional to the energy provided by the APU as the total energy drawn from the battery is fixed. Since the operating power of the APU is almost a constant when it turns on, it can be understood that the energy provided by the APU is inversely proportional to P_M which determines the operating time duration of the APU. Therefore, a larger $Q_{dmd,tot}$ corresponds to a smaller P_M. We have also verified this remark through numerous offline-optimization results as shown in Fig. 6.

3.2. Local aggregated behavior analysis

Optimal charge depletion behavior of a PHEV is influenced by the characteristics of its driving cycle. In order to better understand this influence, we propose to classify the characteristics of a driving cycle into three types based on their different spatial scales: instantaneous, local aggregated average and global. The overarching goal of this paper is to provide fundamental insights for the planning of global SoC trajectories which is mainly determined by the aggregated average behavior of the optimal charge depletion, thus the influence of driving cycle's instantaneous characteristics is neglected. In fact, it is also practically reasonable to do so since accurately predicting the instantaneous characteristics in a long term is extremely hard due to the existence of complex uncertainties in driving behavior and traffic conditions. On the other hand, we can rely on some lower-level adaptive algorithms in online implementations to account for the effects of instantaneous driving conditions while tracking the planned global SoC trajectory [9,15].

In order to examine the influence of the local aggregated average characteristics of the driving cycle on the optimal charge depletion behavior, we segment the entire spatial-domain driving cycle into small basic units (BUs) according to the ordered aggregated characteristics of P_{dmd}^+, a variable that denotes positive P_{dmd}. Specifically, these BUs are determined according to the following two principles: *i*) any two consecutive units have different averages of P_{dmd}^+; *ii*) the variance of P_{dmd}^+ within any unit is sufficiently small. In practical applications, ordered sample clustering algorithms [29] can be employed to fulfill such a segmentation task. Proper segmentation of the driving cycle is closely related with the aggregated characteristics of the optimal charge depletion rates. Therefore, understanding the optimal charge depletion behavior will also facilitate the implementation of the clustering algorithms.

The reason why we only consider positive P_{dmd} when performing the segmentation lies in two facts. First, zero P_{dmd} has no influence on the energy-domain charge depletion rate (CDR) at all. Second, although negative P_{dmd} leads to a totally different CDR than positive P_{dmd} does (*i.e.,* the SoC increases while Q_{dmd} is decreasing), its influence on the aggregated charge depletion behavior can be neglected as it is sparsely scattered along each BU. However, negative P_{dmd} does affect the variations of SoC and Q_{dmd} of each BU. Therefore, we will present a technique to amend its impact on the planning of SoC trajectories in Section 4.

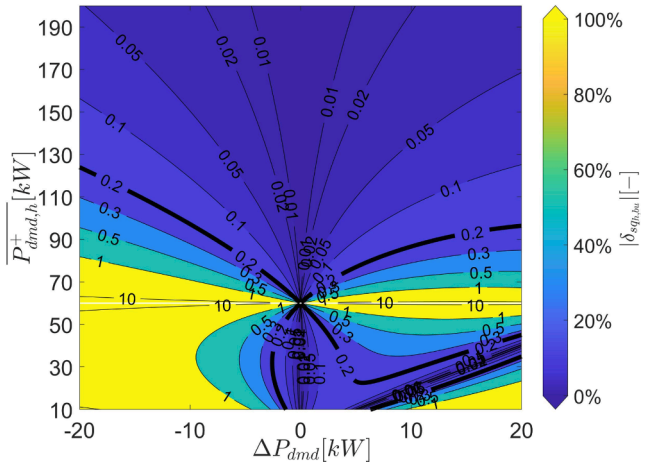

Fig. 9. The relationship between $\delta_{sq_{h,bu}}$ and $\overline{P_{dmd,h}^+}$,ΔP_{dmd}. The contour of $\delta_{sq_{h,bu}} = 0.2$ is thickened to show the large and small quantization borders.

An illustrative P_{dmd} trajectory segmented into multiple BUs is shown in Fig. 7. In this subsection, we will analyze the local aggregated behavior of the optimal charge depletion based on the power characteristics of the BUs. Let us first derive the instantaneous CDRs of different propulsion modes for the PHEV.

By using Eq. (11), the CDR of pure electric mode at each instant can be expressed as:

$$sq_e = \frac{\Delta SoC_e}{\Delta Q_{dmd,e}} = \frac{\Delta SoC_e/\Delta t}{\Delta Q_{dmd,e}/\Delta t} \approx \frac{-\frac{P_{dmd,e}}{V_{oc}Q_{nom}} - \frac{R_0 P_{dmd,e}^2}{V_{oc}^3 Q_{nom}}}{P_{dmd,e}} = -\frac{1}{V_{oc}Q_{nom}}\left(1 + \frac{R_0 P_{dmd,e}}{V_{oc}^2}\right) \tag{23}$$

According to our simulation, the value of sq_e is confined to -4.51 × 10^{-9} ~ -5.04 × 10^{-9}. Therefore, sq_e can be considered as a constant.

Likewise, the instantaneous CDR of hybrid mode can be derived:

$$sq_h = \frac{\Delta SoC_h}{\Delta Q_{dmd,h}} = \frac{\Delta SoC_h/\Delta t}{\Delta Q_{dmd,h}/\Delta t} \approx \frac{-\frac{P_{dmd,h}-P_{apu,1}}{V_{oc}Q_{nom}} - \frac{R_0(P_{dmd,h}-P_{apu,1})^2}{V_{oc}^3 Q_{nom}}}{P_{dmd,h}} = -\frac{P_{dmd,h}-P_{apu,1}}{V_{oc}Q_{nom}P_{dmd,h}}\left(1 + \frac{R_0(P_{dmd,h}-P_{apu,1})}{V_{oc}^2}\right) \tag{24}$$

Therefore, the relationship between CDR and P_{dmd}^+ is shown in Fig. 8.

The relative difference between the instantaneous CDRs of the two modes is:

$$\xi_{eh} = \left|\frac{sq_h - sq_e}{sq_e}\right| = \left|\left(1 - \frac{P_{apu,1}}{P_{dmd,h}}\right)\left(\frac{1 + \frac{R_0(P_{dmd,h}-P_{apu,1})}{V_{oc}^2}}{1 + \frac{R_0 P_{dmd,e}}{V_{oc}^2}}\right) - 1\right| \approx \frac{P_{apu,1}}{P_{dmd,h}} \tag{25}$$

The value of $[1 + R_0(P_{dmd,h} - P_{apu,1})/V_{oc}^2]/(1 + R_0 P_{dmd,e}/V_{oc}^2)$ is very close to 1 (0.947 ~ 1.047) and is thereby ignored. As $P_{apu,1}$ is a constant according to *Lemma* 1, Eq. (25) indicates that ξ_{eh} is an inverse proportional function of $P_{dmd,h}$. Simple calculations show that ξ_{eh} is generally large (greater than 30%), meaning a noticeable difference exists between the CDRs of the two modes. Especially, the difference would be over 100% if $P_{dmd,h}$ is lower than 60 kW. This can be explained by the fact that the optimal CDR is a piece-wise function of P_{dmd} that has a

discontinuity when the working mode changes. Therefore, we need to be careful when $\overline{P^+_{dmd}}$ of a BU is close to P_M, in which case even a small deviation from $\overline{P^+_{dmd}}$ may cause switching of the working mode and further lead to significant change of the CDR. If these small deviations aggregate, as exemplified by basic unit ① in Fig. 7, we need to take the statistical distribution of $P_{dmd,h}$ into consideration in online applications to achieve a better SoC planning.

When $\overline{P^+_{dmd}}$ of a BU is significantly lower than P_M, as exemplified by BU ② in Fig. 7, the charge depletion behavior will be dominated by aggregated pure electric modes. Therefore, the average CDR of this BU can be approximated by sq_e.

On the other hand, when $\overline{P^+_{dmd}}$ of a BU is significantly higher than P_M, the charge depletion behavior will be dominated by aggregated hybrid modes. In this case, the CDR of the BU can be approximated by:

$$sq_{h,bu} \approx sq_h(\overline{P^+_{dmd,bu}}) = -\frac{\overline{P^+_{dmd,bu}} - P_{apu,1}}{V_{oc}Q_{nom}\overline{P^+_{dmd,bu}}}\left(1+\frac{R_0(\overline{P^+_{dmd,bu}} - P_{apu,1})}{V_{oc}^2}\right) \approx -\frac{1}{V_{oc}Q_{nom}}\left(1-\frac{P_{apu,1}}{\overline{P^+_{dmd,bu}}}\right) \tag{26}$$

Table 2
Composition of each trip.

Trips	Composition
Flat trip #1	ChinaCity
Flat trip #2	ChinaCity + US06
Flat trip #3	HWFET + US06 + ChinaCity
Flat trip #4	HWFET + US06 + ChinaCity + UDDS
Hilly trip	ChinaCity + US06

$\frac{R_0(\overline{P^+_{dmd,bu}} - P_{apu,1})}{V_{oc}^2}$, which is close to 0 (-1.26 × 10^{-5} ~ 2.93 × 10^{-5}) according to our simulation, is neglected. The accuracy of the approximation mainly depends on the deviation of the BU's positive P_{dmd} from $\overline{P^+_{dmd,bu}}$ and the sensitivity of $sq_{h,bu}$ to the variation of $\overline{P^+_{dmd,bu}}$, which can be examined by the following perturbation analysis:

$$\delta_{sq_{h,bu}} = \left|\frac{sq_h(\overline{P^+_{dmd,bu}} + \Delta P_{dmd}) - sq_h(\overline{P^+_{dmd,bu}})}{sq_h(\overline{P^+_{dmd,bu}})}\right| \tag{27}$$

By approximating $sq_h(\overline{P^+_{dmd,bu}} + \Delta P_{dmd})$ with its 2nd order Tylor

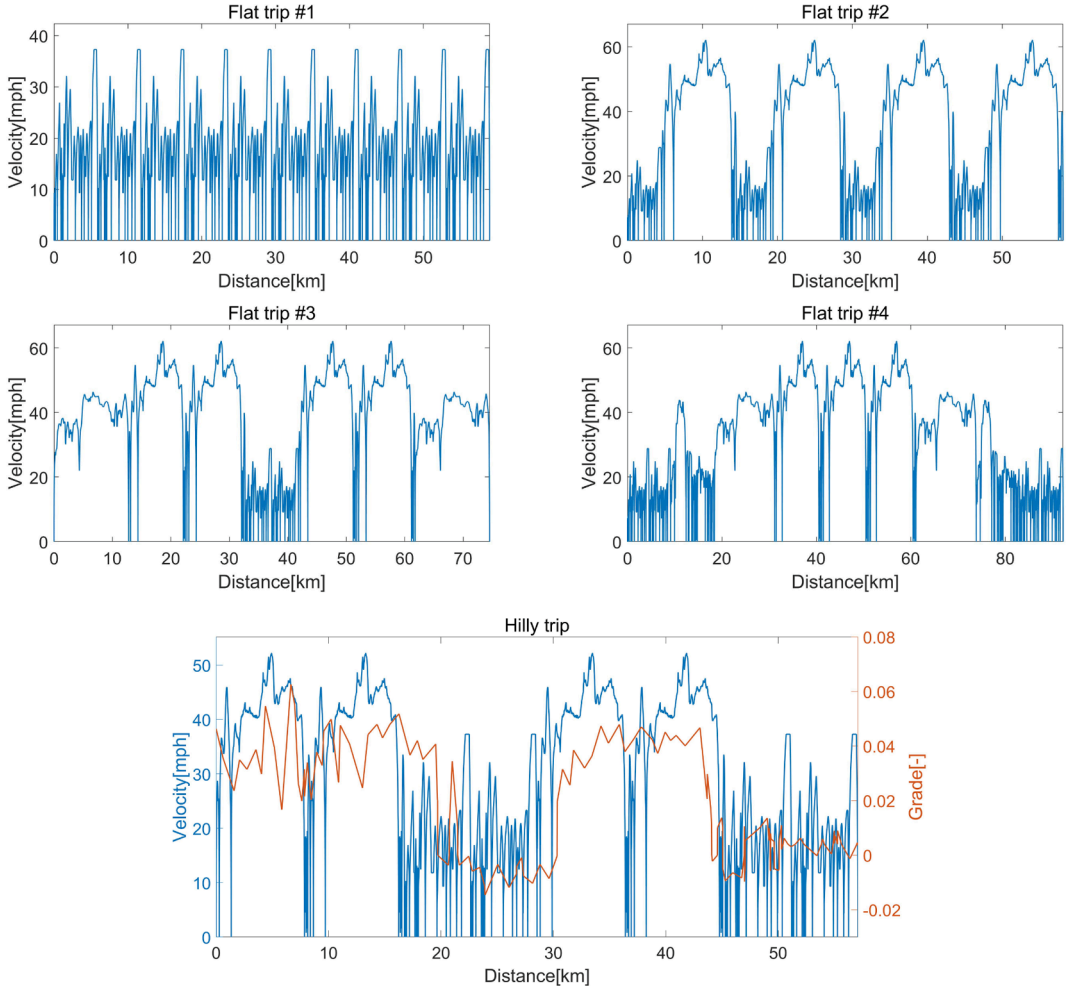

Fig. 10. Speed and grade profiles of the 5 trips used for MiL validation. The slopes of the first 4 trips are equal to zero.

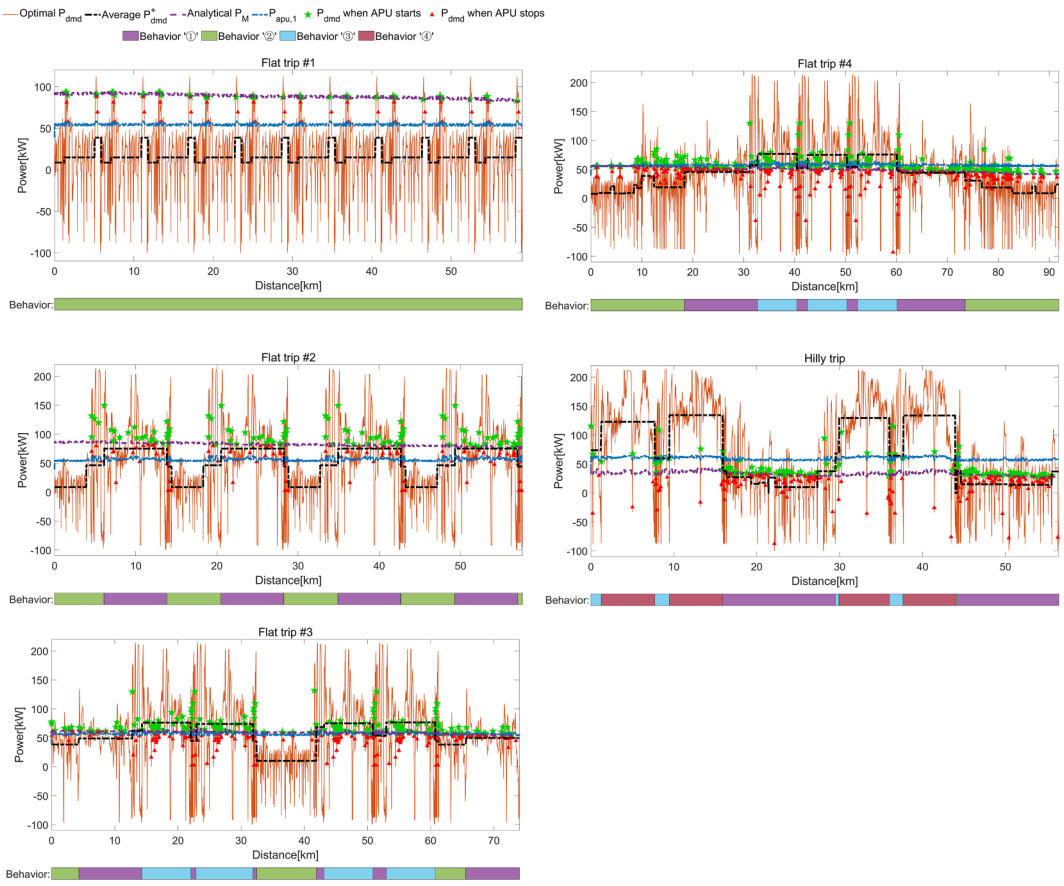

Fig. 11. Comparison of MiL and analytical solution.

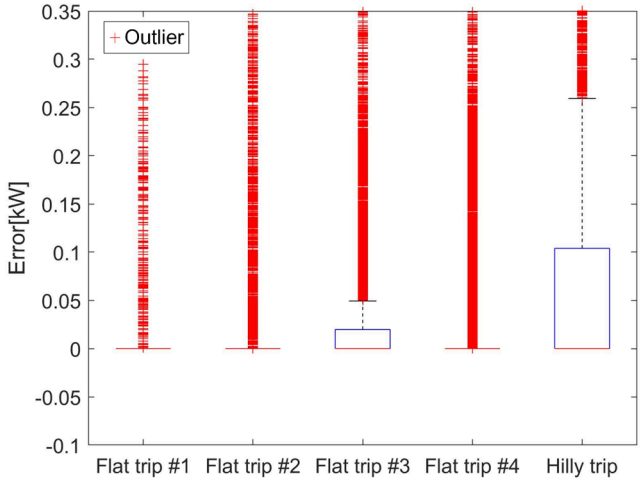

Fig. 12. Boxplot of error between the analytical P^*_{apu} and the P^*_{apu} obtained by the MiL simulations.

expansion, we can further derive that:

$$\delta_{sq_{h,bu}} = \left| \frac{(\overline{P^+_{dmd,bu}} - 2\Delta P_{dmd})\Delta P_{dmd} P_{apu,1}}{\overline{P^+_{dmd,bu}}^2 (\overline{P^+_{dmd,bu}} - P_{apu,1})} \right| \tag{28}$$

The quantitative relationship between $\delta_{sq_{h,bu}}$ and its influencing variables is visualized in Fig. 9, where we can observe that:

i) Basically, $\delta_{sq_{h,bu}}$ decreases with $\overline{P^+_{dmd,bu}}$ but increases with $|\Delta P_{dmd}|$.

ii) The value of $\delta_{sq_{h,bu}}$ is less than 20% in most region. Only when $\overline{P^+_{dmd,bu}}$ is near $P_{apu,1}$ or ΔP_{dmd} is negative and $\overline{P^+_{dmd,bu}}$ is less than $P_{apu,1}$, $sq_{h,bu}$ becomes very sensitive to the variation of $\overline{P^+_{dmd,bu}}$. The high sensitivity implies that small deviations from $\overline{P^+_{dmd,bu}}$ will result in significant changes of the CDR. If these changes aggregate, a different local charge depletion behavior will be formed within the BU. In this case (as illustrated by BU ③ in Fig. 7), we need to consider the distribution of $P_{dmd,h}$ of the BU further to achieve a better SoC planning, On the contrary, the CDR in the low $\delta_{sq_{h,bu}}$ region will maintain relatively stable. (see BU ④ in Fig. 7). The average CDR of this BU can be approximated by sq_h.

3.3. Global behavior analysis

Supposing the entire driving route has been segmented into small BUs with different average CDRs according to the aggregated power characteristics as described above, the global behavior of the optimal charge depletion will exhibit a segment-wise linear pattern in energy domain, which can be further utilized for spatial-domain SoC planning. Generally, online SoC planning based on segment-wise linear charge depletion behavior in energy domain is nontrivial and deserves in-depth investigation in the future. However, when the segment-wise linear behavior becomes globally linear, a simple analytical SoC planning method can be derived, as presented in our previous work of [29]. Based on the aggregated average behavior as analyzed above, we can understand when and why the optimal charge depletion behaves quasi-linear globally:

(1) When the trip is dominated by pure electric modes, *i.e.* $Q_{dmd,tot}$ is small, only a small portion of the BUs are governed by aggregated hybrid modes. Obviously, if these BUs are sparsely located on the trip, the energy-domain SoC trajectory will be approximately linear. Moreover,

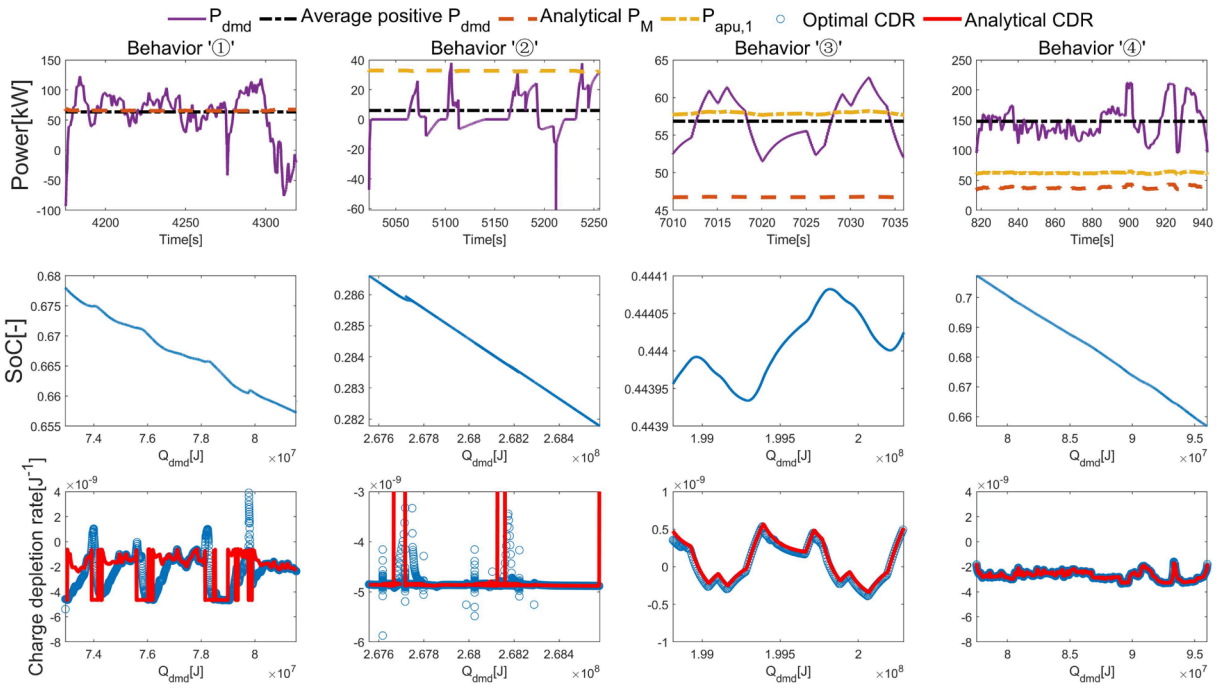

Fig. 13. Power, SoC and CDR trajectories of the four optimal charge depletion behaviors.

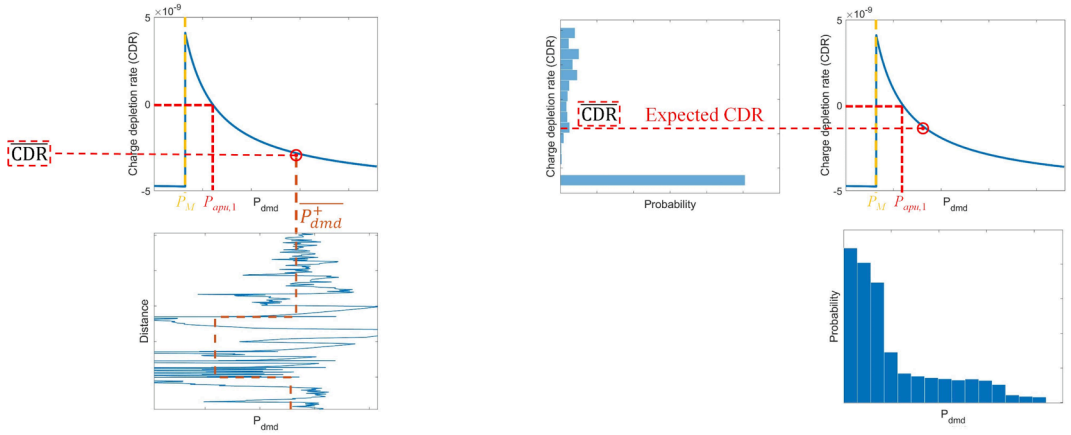

Fig. 14. CDR estimation based on (a) the interpolation of $\overline{P^{+}_{dmd}}$ and (b) the probability distribution of P^{+}_{dmd}.

according to Eq. (25), larger positive driving power of these BUs leads to better global linearity.

(2) When the trip is dominated by hybrid modes, *i.e.* $Q_{dmd,tot}$ is big, it is most likely that the energy-domain global SoC trajectory is nonlinear. However, there is still a chance for the global linearity to appear if the following two conditions are met simultaneously: *i*) the BUs governed by aggregated pure electric modes are sparsely located; *ii*) the average positive power of the basic units governed by aggregated hybrid modes and their differences fall into the region with low $\delta_{sq_{h,bu}}$, as visualized in Fig. 9.

4. Validation and discussions

In this section, we validate the analytical solution to the optimal EM problem, the analysis on the optimal charge depletion behaviors and the associated SoC planning, through MiL simulations. The simulations are performed on an experimentally-validated high-fidelity vehicle

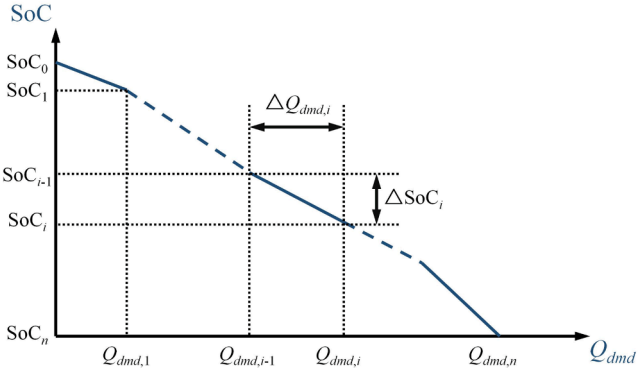

Fig. 15. Estimation principle of the planned SoC trajectory.

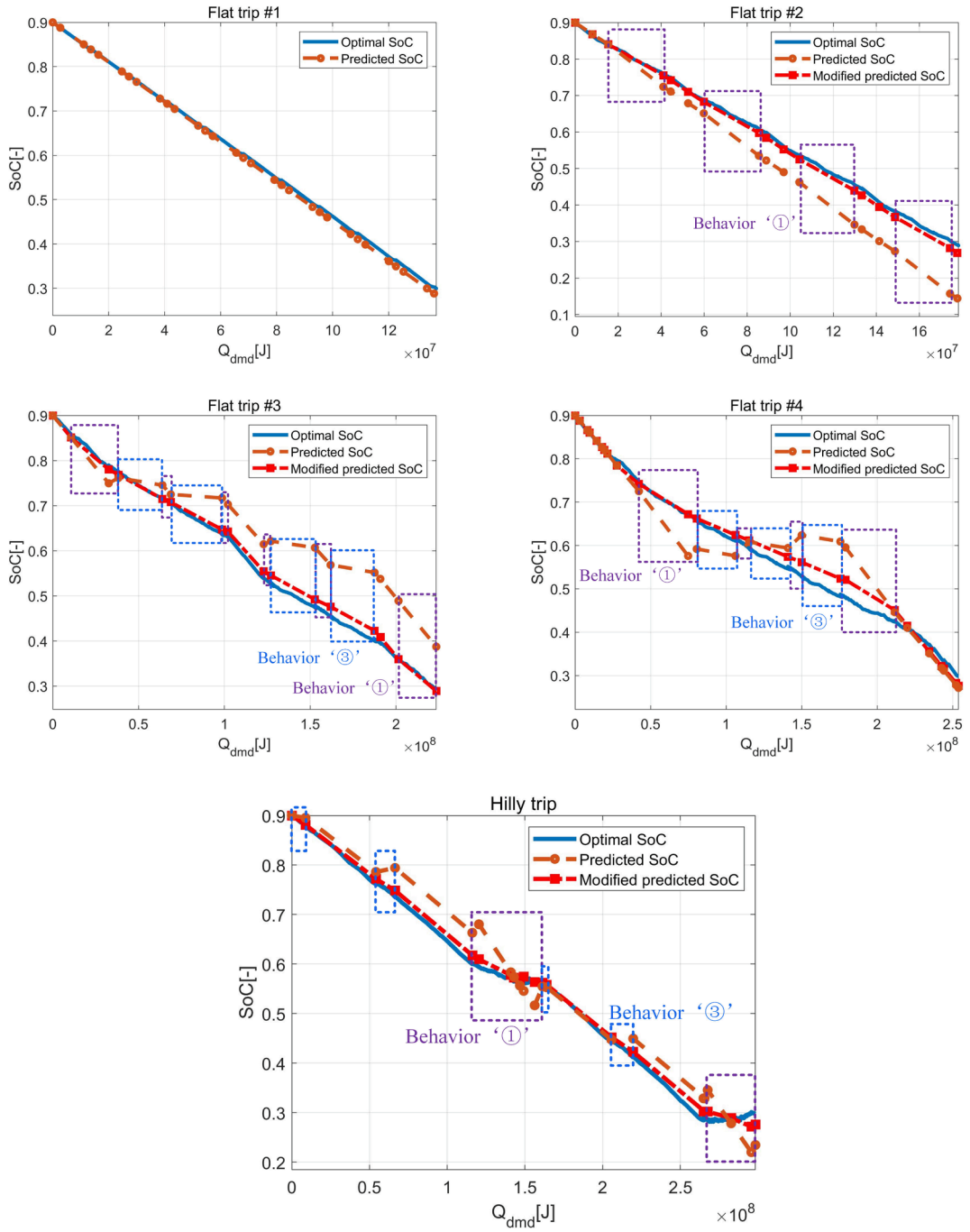

Fig. 16. Comparison of the optimal and planned SoC-Q_{dmd} trajectories. The orange hollow circular markers and the red hollow square markers are the predicted points at the ends of each BU for the originally planned and modified SoC trajectories. The planned SoC trajectories in the purple and blue dotted boxes correspond to the BUs governed by behavior '①' and'③' respectively. The predicted SoC trajectory in orange is planned exactly using Eq. (31) while the slopes of red dot dash lines in the boxes of behavior '①' and '③'are modified by Eq. (33). (For interpretation of the references to colour in this figure legend, the reader is referred to the web version of this article.)

simulator [29], where shooting-based PMP algorithm is applied to obtain the offline optimal solutions. Some critical points are also discussed. We note that it is common practice to employ MiL simulation to verify and validate the design of control strategies before vehicle prototyping in the automotive industry [26,35].

4.1. Validity of the analytical solution

A set of trips composed of standard driving cycles from an open-source database are used to perform the examination. Table 2 summarizes the composition of each trip whose driving profile is shown in Fig. 10. The first four trips simulate driving on flat roads with different traffic conditions, while the last trip simulates driving on undulating terrain. The optimal power trajectories obtained using the high-fidelity simulator for the five trips are shown in Fig. 11.

To verify the validity of the analytically derived optimal power-split policy as expressed by Eq. (17), the results of the two key parameters, *i.e.*, P_{M} and P^{*}_{apu}, obtained using MiL simulations and analytical solutions are compared in Fig. 11 and Fig. 12.

According to the analytical solution, the APU turns on when P_{dmd}

exceeds P_M, and vice versa. Therefore, the P_{dmd} corresponding to the instant when the APU starts/stops is deemed as optimal P_M for the MiL simulations, which is denoted as exact P_M hereafter. As can be seen in Fig. 11, the exact P_M basically oscillates around the analytical P_M. This is because P_{dmd} varies very fast, causing a large jump/drop in its value within even one sampling time of the EM controller (1 s in this study). Consequently, a stable threshold that reflects the APU's start/stop is hard to capture. However, a general range sitting around the analytical P_M can be identified in Fig. 11, validating the effectiveness of the analytical P_M.

The error between the analytical P^*_{apu} and the P^*_{apu} obtained by the MiL simulations is shown in Fig. 12. As can be seen, the error is close to zero except for a few extreme outliers. Again, these outliers are caused by the fast dynamics of P_{dmd} and the slow sampling frequency of the EM controller. Overall, the analytical P^*_{apu} can be considered accurate and effective.

4.2. Validity of optimal charge depletion behaviors

Based on the results of the MiL simulations, four charge depletion behaviors as derived in Section 3.2 are further verified in Fig. 13, where each column belongs to one behavior, and the analytical CDR is equal to sq_e/sq_h (see Eq. (23) and Eq. (24)) when P_{dmd} is lower/higher than the analytical P_M (see Eq. (16)).

The attribute of each behavior is summarized as follows:

a) Behavior '①'. $\overline{P^+_{dmd}}$ is close to P_M. The big fluctuation of the CDR trajectory is caused by the switching of the working modes between pure electric and hybrid modes, which further leads to nonlinearity of the SoC-Q_{dmd} trajectory.

b) Behavior '②'. $\overline{P^+_{dmd}}$ is significantly lower than P_M. This behavior is dominated by pure electric modes. The CDR is rather stable such that the linearity of the SoC-Q_{dmd} trajectory is good.

c) Behavior '③'. $\overline{P^+_{dmd}}$ is close to $P_{apu,1}$, and the locations of $\overline{P^+_{dmd}}$ and ΔP_{dmd} are in the high $\delta_{sq_{h,bu}}$ region (see Fig. 9). Thus, the CDR switches between positive and negative values even when P_{dmd} just has a small change, leading to nonlinearity of the SoC-Q_{dmd} trajectory.

d) Behavior '④'. $\overline{P^+_{dmd}}$ is much larger than $P_{apu,1}$ and the value of $\delta_{sq_{h,bu}}$ is low. The CDR keeps relatively steady such that the linearity of SoC-Q_{dmd} trajectory is good.

Basically, these four behaviors cover the charge depletion behaviors of all the optimal SoC trajectories. The subsequent behavior analysis and SoC planning are based on these four behaviors.

4.3. SoC planning based on optimal charge depletion behaviors

To facilitate the optimal SoC planning and the charge depletion behavior analysis, the above five power trajectories are segmented into BUs with different $\overline{P^+_{dmd}}$, which are plotted by black dot dash lines in Fig. 11. By comparing $\overline{P^+_{dmd}}$, P_M (estimated according to the fitted curve in Fig. 6) and $P_{apu,1}$ (60 kW, according to *Lemma 1*), the charge depletion behavior of each BU can be identified according to the four attributes summarized in the above subsection. The identified behaviors for each driving cycle are shown at the bottom of the power trajectories in Fig. 11. In the following, we will elaborate and validate the SoC planning method using $\overline{P^+_{dmd}}$ and the identified charge depletion behaviors.

The total demanded energy of the i^{th} BU is:

$\Delta Q_{dmd,i} = \Delta Q_{dri,i} - \Delta Q_{reg,i}$ (29) where $\Delta Q_{dri,i}$ and $\Delta Q_{reg,i}$ are the demanded driving energy and the energy recovered through regenerative braking of the i^{th} BU, respectively.

Consequently, the SoC's variation for the i^{th} BU is:

$\Delta SoC_i = \Delta Q_{dri,i} \cdot \overline{\mathrm{CDR}_{dri,i}} - \Delta Q_{reg,i} \cdot \overline{\mathrm{CDR}_{reg,i}}$ (30) where $\overline{\mathrm{CDR}_{dri,i}}$ and $\overline{\mathrm{CDR}_{reg,i}}$ are the average CDR of the i^{th} BU for driving and regenerative braking respectively.

$\overline{\mathrm{CDR}_{dri,i}}$ can be estimated according to CDR curve using $\overline{P^+_{dmd,i}}$, as shown in Fig. 14(a), represented by Eq. (31):

$\overline{\mathrm{CDR}_{dri,i}} = f_{\mathrm{CDR}}(\overline{P^+_{dmd,i}})$ (31)

Since regenerative braking is essentially a pure electric mode, $\overline{\mathrm{CDR}_{reg,i}}$ can be estimated by Eq. (23), which is basically a stable value.

After determining $\Delta Q_{dmd,i}$ and ΔSoC_i, the values of Q_{dmd} and SoC at the end of the i^{th} BU are:

$$\begin{cases} Q_{dmd,i} = \sum_{j=1}^{i} \Delta Q_{dmd,j} \\ SoC_i = SoC_0 + \sum_{j=1}^{i} \Delta SoC_j \end{cases} \quad (32)$$

Consequently, the planned SoC trajectory is formed by connecting a series of points $(Q_{dmd,i}, SoC_i)$ ($i = 0 \sim n$, n is the total number of BUs) using piece-wise lines, as shown in Fig. 15.

In Fig. 16, the planned SoC trajectories (orange dotted lines) are compared with the optimal ones that are obtained by offline MiL optimizations (blue lines). As can be seen, for the last four trips, the planned SoC trajectories have noticeable discrepancy to their optimal counterparts. The deviations are mainly caused by the estimation error in $\overline{\mathrm{CDR}_{dri}}$ of the BUs governed by behaviors '①' and '③', as shown in the dotted box in Fig. 16. When using $\overline{P^+_{dmd}}$ to estimate $\overline{\mathrm{CDR}_{dri}}$, the planned SoC trajectory is likely to exhibit significant error in these two kinds of BUs due to the large variations of their CDRs as shown in Fig. 13. Therefore, the $\overline{\mathrm{CDR}_{dri}}$'s estimation of these two kinds of BUs should be modified. To do so, we propose to estimate the $\overline{\mathrm{CDR}_{dri}}$ of the BUs governed by behaviors '①' and '③' according to the distribution of $P^+_{dmd,i}$:

$\overline{\mathrm{CDR}_{dri,i}} = E(\mathrm{CDR}_{dri,i})$ (33)where $E(\mathrm{CDR}_{dri,i})$ represents the expectation of the distribution of $\mathrm{CDR}_{dri,i}$ that is calculated by the distribution of $P_{dmd,i}$, as shown in Fig. 14b. As can be seen in Fig. 16, after the modification, the planned SoC trajectories have much better matching with the optimal SoC trajectories in the dotted boxes.

From a global perspective, the global linearity of the optimal SoC trajectories of these 5 trips is analyzed by combining Fig. 11 and Fig. 16. For the "Flat trip #1", since it is dominated by pure electric modes, the SoC-Q_{dmd} trajectory has very good linearity. For the last 4 trips, they are dominated by hybrid modes. But the "Flat trip #2" has better linearity due to the sparse distribution of pure electric modes and the low $\delta_{sq_{h,bu}}$ region where $\overline{P^+_{dmd}}$ and ΔP_{dmd} are located. The reason why the linearity for the last three trips deteriorates gradually is due to the dense distribution of pure electric modes and large $\delta_{sq_{h,bu}}$.

5. Conclusions

In this paper, an analytical optimal EM policy is derived for a series PHEV by employing Pontryagin's Minimum Principle, based on which local aggregated behaviors of the optimal CDR in energy domain are analyzed. Four dominant optimal charge depletion behaviors are identified, with whose influencing mechanisms being theoretically revealed and also validated through MiL simulations. It is found that two behaviors have almost constant CDRs due to the fact that they are either dominated by pure electric mode or dominated by hybrid mode, but the CDR is not sensitive to the variation of average driving power. As a result, only average driving power is needed to plan the SoC trajectories for the road segments governed by these two behaviors. On the contrary, the CDRs are quite unstable in the other two behaviors where the powertrain operating mode changes frequently or the CDR is sensitive to the variation of average driving power. To plan the SoC trajectories of the road segments governed by these two behaviors, not only the average driving power but also the driving power's probability distribution is needed. Additionally, based on the local aggregated behavior analysis, prerequisites for good global linearity of the optimal SoC trajectory are also summarized and validated.

Based on the findings of this paper, a computationally efficient near-

optimal SoC planning framework can be designed by intelligently combining data-driven statistics and model-based heuristic rules. However, there are several limitations in our study that hinder its implementation and wide application in the real world. First, the influence of some uncertain factors such as energy recuperation ratio of each road segment and driving power distribution for the desired road segments has not been quantified. Second, the revealed optimal patterns are only applied to series hybrid electric powertrain so far. Its extension to other powertrain configurations needs further study. In the future, we will dedicate ourselves to addressing these limitations to develop high-performance PEM based on the insights gained in this paper.

CRediT authorship contribution statement

Wei Zhou: Conceptualization, Formal analysis, Methodology, Writing – original draft, Writing – review & editing. **Xuan Cai:** Software, Validation, Data curation, Writing – original draft, Visualization. **Yaoqi Chen:** Software, Formal analysis. **Junqiu Li:** Formal analysis. **Xiaoyan Peng:** Conceptualization, Supervision.

Declaration of Competing Interest

The authors declare that they have no known competing financial interests or personal relationships that could have appeared to influence the work reported in this paper.

Acknowledgement

This work is financially supported by the National Natural Science of China (Grant Nos. 51705139,51621004), and the Fundamental Research Funds for the Central Universities.

References

[1] Sun C, Moura SJ, Xiaosong Hu, Hedrick JK, Sun F. Dynamic traffic feedback data enabled energy management in plug-in hybrid electric vehicles. IEEE Trans Contr Syst Technol 2015;23:1075–86. https://doi.org/10.1109/TCST.2014.2361294.
[2] Martinez CM, Hu X, Cao D, Velenis E, Gao B, Wellers M. Energy management in plug-in hybrid electric vehicles: recent progress and a connected vehicles perspective. IEEE Trans Veh Technol 2017;66:4534–49. https://doi.org/10.1109/TVT.2016.2582721.
[3] Zhang F, Hu X, Langari R, Cao D. Energy management strategies of connected HEVs and PHEVs: Recent progress and outlook. Prog Energy Combust Sci 2019;73:235–56. https://doi.org/10.1016/j.pecs.2019.04.002.
[4] Liu J, Chen Y, Li W, Shang F, Zhan J. Hybrid-trip-model-based energy management of a PHEV with computation-optimized dynamic programming. IEEE Trans Veh Technol 2018;67:338–53. https://doi.org/10.1109/TVT.2017.2777852.
[5] Hongwen H, Jinquan G, Jiankun P, Huachun T, Chao S. Real-time global driving cycle construction and the application to economy driving pro system in plug-in hybrid electric vehicles. Energy 2018;152:95–107. https://doi.org/10.1016/j.energy.2018.03.061.
[6] Xu N, Kong Y, Yan J, Zhang Y, Sui Y, Ju H, et al. Global optimization energy management for multi-energy source vehicles based on “Information layer - Physical layer - Energy layer - Dynamic programming” (IPE-DP). Appl Energy 2022;312:118668. https://doi.org/10.1016/j.apenergy.2022.118668.
[7] Lei Z, Sun D, Liu J, Chen D, Liu Y, Chen Z. Trip-oriented model predictive energy management strategy for plug-in hybrid electric vehicles. IEEE Access 2019;7:113771–85. https://doi.org/10.1109/ACCESS.2019.2933015.
[8] Zhang C, Vahidi A. Route preview in energy management of plug-in hybrid vehicles. IEEE Trans Contr Syst Technol 2012;20:546–53. https://doi.org/10.1109/TCST.2011.2115242.
[9] Zhou W, Zhang C, Li J, Fathy HK. A pseudospectral strategy for optimal power management in series hybrid electric powertrains. IEEE Trans Veh Technol 2016;65:4813–25. https://doi.org/10.1109/TVT.2015.2466671.
[10] Climent H, Pla B, Bares P, Pandey V. Exploiting driving history for optimising the Energy Management in plug-in Hybrid Electric Vehicles. Energy Convers Manage 2021;234:113919. https://doi.org/10.1016/j.enconman.2021.113919.
[11] Cordiner S, Galeotti M, Mulone V, Nobile M, Rocco V. Trip-based SOC management for a plugin hybrid electric vehicle. Appl Energy 2016;164:891–905. https://doi.org/10.1016/j.apenergy.2015.06.009.
[12] Guo N, Zhang X, Zou Y, Guo L, Du G. Real-time predictive energy management of plug-in hybrid electric vehicles for coordination of fuel economy and battery degradation. Energy 2021;214:119070. https://doi.org/10.1016/j.energy.2020.119070.
[13] Xie S, Hu X, Xin Z, Li L. Time-efficient stochastic model predictive energy management for a plug-in hybrid electric bus with an adaptive reference state-of-charge advisory. IEEE Trans Veh Technol 2018;67:5671–82. https://doi.org/10.1109/TVT.2018.2798662.
[14] Tang X, Jia T, Hu X, Huang Y, Deng Z, Pu H. Naturalistic data-driven predictive energy management for plug-in hybrid electric vehicles. IEEE Trans Transp Electrific 2021;7:497–508. https://doi.org/10.1109/TTE.2020.3025352.
[15] Onori S, Tribioli L. Adaptive Pontryagin’s Minimum Principle supervisory controller design for the plug-in hybrid GM Chevrolet Volt. Appl Energy 2015;147:224–34. https://doi.org/10.1016/j.apenergy.2015.01.021.
[16] Padmarajan BV, McGordon A, Jennings PA. Blended rule-based energy management for PHEV: System structure and strategy. IEEE Trans Veh Technol 2016;65:8757–62. https://doi.org/10.1109/TVT.2015.2504510.
[17] Yang C, Du S, Li L, You S, Yang Y, Zhao Y. Adaptive real-time optimal energy management strategy based on equivalent factors optimization for plug-in hybrid electric vehicle. Appl Energy 2017;203:883–96. https://doi.org/10.1016/j.apenergy.2017.06.106.
[18] Zhang Y, Liu H, Zhang Z, Luo Y, Guo Q, Liao S. Cloud computing-based real-time global optimization of battery aging and energy consumption for plug-in hybrid electric vehicles. J Power Sources 2020;479:229069. https://doi.org/10.1016/j.jpowsour.2020.229069.
[19] Montazeri-Gh M, Pourbafarani Z. Near-optimal SOC trajectory for traffic-based adaptive PHEV control strategy. IEEE Trans Veh Technol 2017;66:9753–60. https://doi.org/10.1109/TVT.2017.2757604.
[20] Min Q, Li J, Liu B, Li J, Sun F, Sun C. Guided model predictive control for connected vehicles with hybrid energy systems. Energy 2021;230:120780. https://doi.org/10.1016/j.energy.2021.120780.
[21] Tianheng F, Lin Y, Qing G, Yanqing H, Ting Y, Bin Y. A supervisory control strategy for plug-in hybrid electric vehicles based on energy demand prediction and route preview. IEEE Trans Veh Technol 2015;64:1691–700. https://doi.org/10.1109/TVT.2014.2336378.
[22] Schori M, Boehme TJ, Jeinsch T, Schultalbers M. A robust predictive energy management for plug-in hybrid vehicles based on hybrid optimal control theory. 2015 American Control Conference (ACC), Chicago, IL, USA: IEEE; 2015, p. 2278–83. 10.1109/ACC.2015.7171072.
[23] Pourbafarani Z, Montazeri-Gh M, Khasheinejad M. Improvement of PHEV equivalent fuel economy and battery life by applying traffic-based SOC management. IEEE Trans Transp Electrific 2021. https://doi.org/10.1109/TTE.2021.3109083.
[24] Chen D, Kim Y, Stefanopoulou AG. State of Charge Node Planning with Segmented Traffic Information. 2018 Annual American Control Conference (ACC), Milwaukee, WI, USA: IEEE; 2018, p. 4969–74. 10.23919/ACC.2018.8431103.
[25] Schmid R, Buerger J, Bajcinca N. Energy management strategy for plug-in-hybrid electric vehicles based on predictive PMP. IEEE Trans Contr Syst Technol 2021;29:2548–60. https://doi.org/10.1109/TCST.2020.3048129.
[26] Ekhtiari S, Faieghi M, Azad NL. Sensitivity analysis of a real-time trip planning assisted energy management system for connected plug-in hybrid electric vehicles. IEEE Trans Veh Technol 2019;68:7340–52. https://doi.org/10.1109/TVT.2019.2922158.
[27] Hai Y, Ming K, McGee R. Trip-oriented energy management control strategy for plug-in hybrid electric vehicles. IEEE Trans Contr Syst Technol 2014;22:1323–36. https://doi.org/10.1109/TCST.2013.2278684.
[28] Yu H, Tseng F, McGee R. Driving pattern identification for EV range estimation. 2012 IEEE International Electric Vehicle Conference, Greenville, SC, USA: IEEE; 2012, p. 1–7. 10.1109/IEVC.2012.6183207.
[29] Zhou W, Chen Y, Zhai H, Zhang W. Predictive energy management for a plug-in hybrid electric vehicle using driving profile segmentation and energy-based analytical SoC planning. Energy 2021;220:119700. https://doi.org/10.1016/j.energy.2020.119700.
[30] Mahmoodi-k M, Montazeri M, Madanipour V. Simultaneous multi-objective optimization of a PHEV power management system and component sizing in real world traffic condition. Energy 2021;233:121111. https://doi.org/10.1016/j.energy.2021.121111.
[31] Zhou W, Zhang N, Zhai H. Enhanced battery power constraint handling in MPC-based HEV energy management: a two-phase dual-model approach. IEEE Trans Transp Electrific 2021;7:1236–48. https://doi.org/10.1109/TTE.2021.3056681.
[32] Zhang Q, Wu K, Shi Y. Route planning and power management for PHEVs with reinforcement learning. IEEE Trans Veh Technol 2020;69:4751–62. https://doi.org/10.1109/TVT.2020.2979623.
[33] Lv C, Zhang J, Li Y, Yuan Y. Mechanism analysis and evaluation methodology of regenerative braking contribution to energy efficiency improvement of electrified vehicles. Energy Convers Manage 2015;92:469–82. https://doi.org/10.1016/j.enconman.2014.12.092.
[34] Kim N, Rousseau A, Lee D. A jump condition of PMP-based control for PHEVs. J Power Sources 2011;196:10380–6. https://doi.org/10.1016/j.jpowsour.2011.07.003.
[35] Zhou S, Chen Z, Huang D, Lin T. Model prediction and rule based energy management strategy for a plug-in hybrid electric vehicle with hybrid energy storage system. IEEE Trans Power Electron 2021;36:5926–40. https://doi.org/10.1109/TPEL.2020.3028154.